Thermodynamic and Transport Properties of Single Crystal $YbNi_4Cd$

by

Jeonghun Lee

B.A.Sc., University of Waterloo, 2016

Thesis Submitted in Partial Fulfillment o f the
Requirements for the Degree of
Master of Science

in the
Department of Physics
Faculty of Science

SIMON FRASER UNIVERSITY
Summer 2018

Approval

Name:	**Jeonghun Lee**
Degree:	**Master of Science (Physics)**
Title:	**Thermodynamic and Transport Properties of Single Crystal $YbNi_4Cd$**
Examining Committee:	**Chair:** Malcolm Kennett Associate Professor
	Eundeok Mun Senior Supervisor Assistant Professor
	J. Steven Dodge Supervisor Associate Professor
	David Broun Internal Examiner Associate Professor
Date Defended:	**July 20, 2018**

Abstract

The single crystal growth and the physical properties of the rare-earth based ternary intermetallic compounds RNi$_4$Cd (R = Y and Yb) will be presented. The powder X-ray diffraction measurement reveals that these compounds crystallize in the face-centered cubic (fcc), MgCu$_4$Sn-type structure (space group $F\bar{4}3m$). Magnetization, electrical resistivity, and specific heat measurements are used to study thermodynamic and transport properties of YbNi$_4$Cd. The magnetic susceptibility shows that $4f$ electrons of Yb^{3+} ions are well localized. The electrical resistivity and specific heat measurements show antiferromagnetic ordering below $T_N = 0.97$ K. Applying a field along the [111] direction results in the suppression of T_N below 0.4 K at the critical field $H_c \sim 4.5$ kOe. No non-Fermi liquid behavior is observed in the vicinity of H_c. Above H_c, the magnetoresistivity shows an unconventional temperature dependence $\rho(T) = \rho_0 + AT^n$ with $n > 2$, suggesting that an additional scattering mechanism in the resistivity needs to be considered. Based on the analysis of experimental results, we conclude that the Yb^{3+} moments and conduction electrons are weakly coupled. Despite the antiferromagnetic ordering below T_N, YbNi$_4$Cd exhibits a large frustration parameter $|\theta_p/T_N| \sim 16$, where the magnetic Yb^{3+} ions occupy the tetrahedra on the fcc lattice.

Keywords: Physical properties; Rare-earth intermetallics; Heavy Fermion; Magnetism

Dedication

To my parents.

Acknowledgements

I would like to thank my senior supervisor Eundeok Mun for providing me the opportunity to work at Emerging Material Lab and guiding me through the graduate studies. He taught me how to conduct research covering a broad aspects from crystal growth to publication. He also helped me preparing a presentation and giving a talk at a conference-level setting. Again, I am grateful for his support. Also, I would like to thank my supervisor J. Steven Dodge who has provided me valuable advices on my research during the annual progress committee meeting as well as the correction of this thesis. I would also like to thank my lab members and co-students at other lab for providing me valuable information on course materials and research. Lastly, I would like to thank professors who taught physics courses and student seminar courses which helped me a lot in conducting an oral presentation.

Table of Contents

List of Tables

List of Figures

Chapter 1

Introduction

1.1 The Scope of This Thesis

Among the intermetallic compounds, the rare-earth-based intermetallics are particularly of interest due to the variety of exotic phenomena that they exhibit, such as the magnetocaloric effect [1], unconventional superconductivity [2], multiferroicity [3], and heavy fermion behavior [4]. These phenomena depend on the interplay between structure and electrical and magnetic properties. Thus, understanding structure and electronic and magnetic properties of an pristine single crystal of intermetallic compound is the first stage of discovering novel phenomena.

We have grown single-crystal $YbNi_4Cd$ for the first time. The crystal structure of RNi_4Cd has been reported by other group [5], but no thermodynamic and transport properties have been studied at the time of writing this thesis. Thus, we have published its thermodynamic and transport properties, and this thesis will be based on the publication with background information [6]. Theoretical background and general information about rare-earth-based intermetallic compounds will be presented in the following sections of this chapter. Both the temperature- and field-dependent specific heat and resistivity have been studied, and the experiment procedure and the obtained results will be presented in Chapter 2. Chapter 3 is dedicated to the analysis of the experimental results. In this chapter, the $H - T$ phase diagram of $YbNi_4Cd$ will be presented, and anomalous behavior in the electrical resistivity and the specific heat will be discussed. Conclusions and future directions for study will be discussed in Chapter 4.

1.2 Single Crystal Growth

A perfect single crystal is commonly referred to as a single solid piece in which the simplest constituents, the atoms or molecules, are arranged periodically in a lattice where specific geometrical symmetry operations are valid inside the whole piece. Polycrystalline material is made up of many micrometer-sized single crystals which are also called *crystallites* or

grains, and these crystallites have no preferred orientation with respect to each other. The crystallinity of a material is important for characterizing it because its physical properties change dramatically depending on the degree of crystallinity. For example, electrical, thermal, and magnetic properties can be affected significantly by grain boundaries in polycrystalline materials [7]. The preparation of a single crystal with sufficient size requires understanding of phase relations and different stages in the crystallization processes [8].

There are a number of single crystal growth methods used in solid-state research. One method is the floating zone (FZ) melting technique (melt growth). The floating zone technique does not require the use of a crucible, avoiding contamination from the crucible. However, this method is used in cases where starting materials melt congruently and involves temperature gradients for crystal growth. Another popular method is flux growth. The flux growth method requires the use of a crucible to hold the constituent elements and flux. The temperature is raised to allow the mixture to melt and become a homogeneous molten solution at high temperatures. At this stage, the solution is supersaturated, and the desired product precipitates out from the solution as the crucible is cooled slowly. The material of crucible must be chosen carefully so that it does not react with the solution [9]. The advantage of this technique is that the flux increases the rate of the diffusion of the elements in its mixture at a temperature lower than the melting point of the constituents themselves, and the rate of reaction can be tuned by controlling the temperature, pressure, and the ratio of constituent elements. Once the desired product is separated from the flux, it is possible to remove excess flux on the surface by polishing or chemical etching. Another advantage is that single crystals grown by the flux method show natural facets, which makes it easier to measure anisotropic physical properties. The main disadvantage is the low growth rate, which is generally much slower than that of the melt growth method. Despite the long growing time, the flux method is widely used in a laboratory setting due to its accessibility. We used the flux method to grow the single crystals of $R\mathrm{Ni}_4\mathrm{Cd}$ (R = Y and Yb) [10, 11].

1.3 Powder X-ray Diffraction Crystallography

Since the discovery of X-ray diffraction from crystals by Max von Laue in 1912 and by W.L Bragg and W.H Bragg in 1913, X-ray diffraction (XRD), along with neutron diffraction, have become important tools to characterize materials. X-ray crystallography is a well-established field and many excellent books about X-ray diffraction crystallography are available [12, 13].

Atoms or molecules in crystal structure can be represented as points, and the resulting three-dimensional array of points can be simplified to a primitive cell, a minimum volume cell which satisfies translation symmetry, defined by the three primitive vectors $\vec{a}$, $\vec{b}$, and $\vec{c}$. Typically, the lengths of each primitive vector, also known as lattice parameters, are denoted as a, b, and c, respectively and the angles between $\vec{b}$ and $\vec{c}$, $\vec{a}$ and $\vec{c}$, and, $\vec{a}$ and

$\vec{b}$ are denoted as α, β, and γ, respectively. There are only seven possible crystal systems: cubic, tetragonal, orthorhombic, hexagonal, rhombohedral, monoclinic, and triclinic, each of which has different relations among parameters. There are 14 Bravais lattices, each of which fills space without overlapping. The seven crystal systems, six parameters which define them, and 14 Bravais lattices with lattice symbols which classify them are given in Table 1.1. In addition to these seven crystal systems, the point group symmetry operations such as reflection, rotation and rotoinversion, and the screw axis and glide plane symmetry operation give rise to 230 different space groups. The list of all 230 space groups can be found elsewhere [9].

Table 1.1: Seven crystal systems with 14 Bravais lattices.

Crystal System	Six Parameters	Bravais Lattices
Cubic	$a = b = c; \alpha = \beta = \gamma = 90^\circ$	Primitive (P) Face Centered (F) Body Centered (I)
Orthorhombic	$a \neq b \neq c; \alpha = \beta = \gamma = 90^\circ$	Primitive (P) Face Centered (F) Body Centered (I) Base Centered (C)
Tetragonal	$a = b \neq c; \alpha = \beta = \gamma = 90^\circ$	Primitive (P) Body Centered (I)
Monoclinic	$a \neq b \neq c; \alpha = \gamma = 90^\circ \beta \neq 90^\circ$	Primitive (P) Base Centered (C)
Rhombohedral	$a = b = c; \alpha = \beta = \gamma \neq 90^\circ$	Primitive (P)
Triclinic	$a \neq b \neq c; \alpha \neq \beta \neq \gamma \neq 90^\circ$	Primitive (P)
Hexagonal	$a = b \neq c; \alpha = \beta = 90^\circ \gamma = 120^\circ$	Primitive (P)

Nearly all crystals fall into one of 230 space groups, and the powder X-ray diffraction instrument ultimately allows one to determine the space group and the atomic spacings, thus the lattice parameters.

The principle behind X-ray diffraction is that reflection due to the constructive interference occurs when a monochromatic X-ray is incident on a crystalline sample with Bragg conditions

$$n\lambda = 2d \sin\theta, \tag{1.1}$$

where n is the n^{th} order reflection, λ is the wavelength of the incident X-ray beam, d is the interplanar spacing, and θ is the angle between the incident X-ray beam and the normal to the reflection plane. For this condition to be satisfied, the wavelength must be comparable to the interplanar distance, which is why X-rays are used. The angle between the diffracted X-ray beam and the transmitted beam is 2θ, defined as the diffraction angle. The detector

in the instrument records the intensities by scanning through a range of 2θ. For a cubic crystal structure with lattice parameter a, the interplanar spacing d is given by

$$\frac{1}{d^2} = \frac{h^2 + k^2 + l^2}{a^2}, \tag{1.2}$$

where h, k, and l are the Miller indices of the diffracting planes. Similar relationships are available for other six crystal systems.

For our X-ray diffraction measurements, we grind the single crystals into a powder to produce an equal distribution of every possible crystalline orientations. The relative intensities in the resulting pattern depend on the atomic constituents, and the positions of the peaks depend only on its crystal structure. These combined characteristics in the X-ray diffraction pattern serve as a *fingerprint* for a crystal. This diffraction pattern from a single kind of crystal structure is also called the *phase*. In general, the powder X-ray diffraction is also used to identify different or unknown phases within a sample. Given the diffraction pattern of a powdered sample, one can identify the presence of other phases in the sample and the crystal structure of an unknown phase by matching the unknown diffraction pattern to the known pattern in the database such as International Center for Diffraction Data (ICDD).

1.4 Curie-Weiss Paramagnetism

The quantity which describes the responsiveness to an applied magnetic field is the magnetic susceptibility, which is defined as $\chi = M/H$, where M is the magnetization and H is the applied field. In paramagnetic materials, electrons give rise to non-zero moments and these moments are treated independently because they interact weakly at high temperatures. At sufficiently high temperature these individual magnetic moments fluctuate and point in random directions, which results in the zero net magnetization $M = 0$. The interaction of these moments becomes dominant over thermal fluctuation at sufficiently low temperature and high magnetic field. Thus, the degree of magnetization has the temperature and magnetic field dependence. Upon cooling the magnetic material, there is a magnetic transition at the magnetic ordering temperature T_M. When $T \gg T_M$, the magnetic susceptibility can be described by the Curie-Weiss law:

$$\chi = \frac{M}{H} = \frac{N\mu_{eff}^2}{3k_B(T - \theta_P)} = \frac{C}{T - \theta_P}, \tag{1.3}$$

where N is the number of magnetic atoms per unit volume, μ_{eff} is the effective moment, C is the Curie constant, and θ_P is the Weiss temperature. The dimensionless quantity χ is the susceptibility per unit volume. μ_{eff} is defined as $\mu_{eff} = p\mu_B$, where μ_B is Bohr magneton and p is the effective number of Bohr magnetons, $p = g[J(J+1)]^{1/2}$, where g is the Landé

g-factor, given by

$$g = 1 + \frac{J(J+1) + S(S+1) - L(L-1)}{2J(J+1)}. \tag{1.4}$$

The inverse magnetic susceptibility of a magnetic material at sufficiently high temperatures is linear in temperature. By extrapolating the inverse magnetic susceptibility as a function of temperature to low temperature, the Weiss temperature θ_p, can be obtained from the T-intercept, and the sign of this value is associated with the type of the interaction between moments. Typically, for $\theta_p > 0$ these moments experience a net ferromagnetic interaction and for $\theta_p < 0$ they experience a net antiferromagnetic interaction, where $\theta_p = 0$ indicates that these moments behave like a paramagnet. The temperatures at which the ferro- and antiferro-magnetic transitions occur are known as the Curie temperature T_C and Néel temperature T_N, respectively.

1.5 RKKY Interaction

A long-range magnetic order which occurs in metallic rare-earth-based intermetallic compounds can be explained by the Ruderman-Kittel-Kasuya-Yoshida (RKKY) interaction. The overlap between $4f$ orbital wavefunctions from adjacent rare-earth atoms is small, thus the direct exchange interaction is rather difficult. These localized $4f$ electrons in rare-earth atoms interact indirectly by coupling through conduction electrons. The exchange coupling of the RKKY interaction is weaker than that of the direct exchange interaction and oscillates in signs as the distance r between magnetic ions increases. The RKKY exchange coupling is given by

$$J_{RKKY} = J_0(r)\cos(2k_F r), \tag{1.5}$$

where J_0 is the RKKY coefficient which decays as r^3 and k_F is the Fermi wave vector, $k_F = (3\pi^2 n)^{1/3}$.

1.6 Rare-earth Intermetallic Compounds

Rare-earth-based intermetallic compounds have special properties in that $4f$ electrons in rare earth elements are localized inside the $5s^2 5p^6$ shell, and the effective moments of rare-earth ions predicted theoretically using the ground state of configuration agrees well with those obtained from experiments. In general, both metallic and insulating rare-earth intermetallic compound have localized moments. Most of rare-earth elements or lanthanide series are trivalent with a few exceptions and their chemical properties are similar. Because $4f$ electrons lie inside the $5s$ and $5p$ in lanthanides, which causes the poor screening, this gives rise to the systematic decrease in atomic distances as the atomic number increases, which is known as the lanthanide contraction. In this respect, the choice of rare-earth elements in intermetallic compounds can serve as a parameter as it alters the distance-dependent

interactions such as RKKY interactions; thus tuning the electrical and magnetic properties while conserving its stoichiometric ratio and crystal structure. The general magnetic properties of lanthanide series are listed in Table 1.2.

Table 1.2: Magnetic properties of lanthanide series.

$4f$ e^-	$[R^{3+}]$	S[a]	L[b]	J[c]	g[d]	gJ[e]	$2J+1$[f]	$R\ln(2J+1)$[g]	$p_{calc.}$[h]
0	La	0	0	0	–	–	–	–	–
1	Ce	1/2	3	5/2	6/7	15/7	6	14.90	2.54
2	Pr	1	5	4	4/5	16/5	9	18.27	3.58
3	Nd	3/2	6	9/2	8/11	36/11	10	19.14	3.62
4	Pm	2	6	4	3/5	12/5	9	18.27	2.68
5	Sm	5/2	5	5/2	2/7	5/7	6	14.90	0.84
6	Eu	3	3	0	–	–	–	–	0
7	Gd	7/2	0	7/2	2	7	8	17.29	7.94
8	Tb	3	3	6	3/2	9	13	21.33	9.72
9	Dy	5/2	5	15/2	4/3	10	16	23.05	10.63
10	Ho	2	6	8	5/4	10	17	23.56	10.60
11	Er	3/2	6	15/2	6/5	9	16	23.05	9.59
12	Tm	1	5	6	7/6	7	13	21.33	7.57
13	Yb	1/2	3	7/2	8/7	4	8	17.29	4.54
14	Lu	0	0	0	–	–	–	–	–

[a]Spin angular momentum S
[b]Orbital angular momentum L
[c]Total angular momentum J obtained by Hund's rule: $J = |L - S|$ when $4f$ shell is filled less than half full and $J = |L + S|$ when filled more than half full
[d]g is the Landé g-factor, $g = 1 + \frac{J(J+1)+S(S+1)-L(L-1)}{2J(J+1)}$
[e]Saturated moment, $\mu_{sat} = gJ$
[f]$(2J+1)$-$fold$ degeneracy in the absence of external fields
[g]Magnetic entropy S_m, where R is 8.3144598 J K^{-1} mol^{-1}.
[h]Effective Bohr Magnetons $p_{calc.} = g[J(J+1)]^{1/2}$

1.7 Specific Heat: Lattice and Electronic Contributions

Specific heat measurements provide useful information about the lattice, electronic, and magnetic properties of a solid. It also provides information about structural, magnetic, and superconducting phase transitions. It can also be used to detect an unwanted second phase in the crystal. The heat capacity at fixed pressure is given by

$$C_p = \left(\frac{dQ}{dT}\right)_p. \tag{1.6}$$

Because heat capacity is an extensive variable, it is often expressed as molar specific heat. In ordinary metals, the electron and lattice contributions are dominant at low temperatures,

and the specific heat at low temperatures is given by

$$C_p(T) = \underbrace{\gamma T}_{\text{electronic}} + \underbrace{\beta T^3}_{\text{lattice}}, \tag{1.7}$$

where γ and β are electronic and lattice specific heat coefficients, respectively. The temperature dependence of each contribution can be obtained from the free electron gas model and the Debye model. The electronic specific heat coefficient is associated with the conduction band density of states at the Fermi level. From γ, the Fermi energy can be estimated by $\gamma = {}^{\pi^2 k_B^2}/_{E_F}$, where k_B is the Boltzmann constant and E_F is the Fermi energy. From β, the Debye temperature θ_D can be estimated by $\beta = {}^{12\pi^4 k_B}/_{5\theta_D}$. In the limit of high temperature, the specific heat reaches the Dulong-Petit limit $3N_A k_B T$ due to the equipartition theorem, where N_A is the Avogadro's number.

1.8 Schottky Anomaly

Specific heat measurements on rare-earth-based intermetallic compounds provide useful information about their magnetic properties. For an isolated rare-earth element with total angular momentum J, it has $(2J+1)$-fold degenerate levels. In the presence of an electric or magnetic field, these levels are lifted. A Schottky anomaly, a peak in magnetic specific heat, can be observed when the CEF levels are populated. The full magnetic entropy $N_A k_B \ln(2J+1)$ has to be recovered at high temperatures. A quantitative interpretation of the temperature-dependent specific heat and magnetic entropy requires the knowledge of actual CEF splitting levels and CEF parameters [14]. The splitting energies due to CEF can also be studied by inelastic neutron scattering. To extract the magnetic part of the specific heat, one can subtract the total specific heat of a non-magnetic compound, obtained through La, Y or Lu substitution, from that of the magnetic compound. For a multi-level system, the general expression for a Schottky anomaly is given by

$$C_{Sch}(T) = k_B \beta^2 \frac{\sum_{i,j} g_i g_j E_i (E_i - E_j) e^{-\beta(E_i+E_j)}}{\left[\sum_i g_i e^{-\beta E_i}\right]^2}, \tag{1.8}$$

where g is the degeneracy and E is the energy of the i^{th} level.

For a system of two levels separated by the energy gap Δ with degeneracies g_0 and g_1, the specific heat due to a Schottky anomaly is

$$C_{Sch}^{two-level}(T) = k_B (\beta\Delta)^2 \frac{g_0}{g_1} \frac{e^{\beta\Delta}}{\left[1 + (g_0/g_1) e^{\beta\Delta}\right]^2}. \tag{1.9}$$

The specific heat due to a Schottky anomaly for a two-level system with several g_1/g_0 values is plotted in Fig. 1.1. When two levels are equally degenerate, the maximum specific heat occurs at $T \simeq 0.42\Delta/k_B$. When the excited level is more degenerate ($g_1/g_0 = 2$),

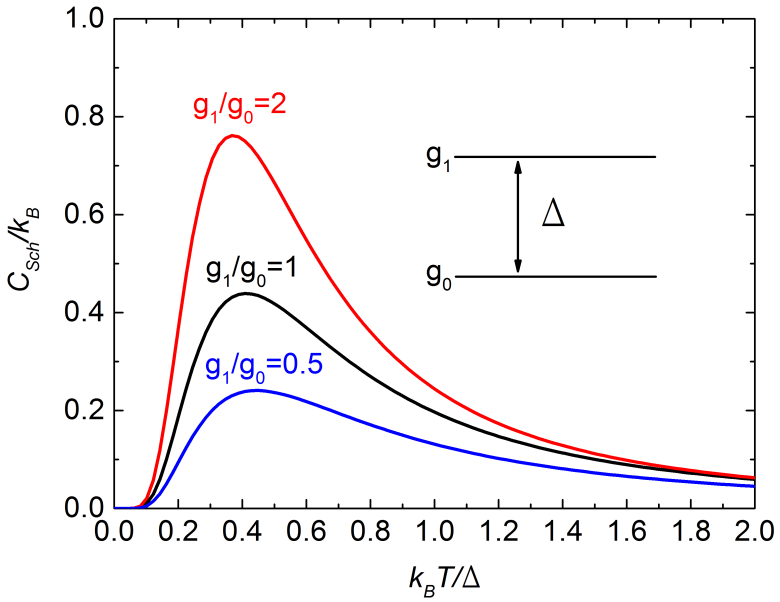

Figure 1.1: Specific heat due to Schottky anomaly for a two-level system with $g_1/g_0 = 0.5$, 1, and 2.

the magnitude of specific heat is higher than that of the equally degenerate case, and the maximum occurs at a slightly lower temperature ($T \simeq 0.38\Delta/k_B$). When the ground level is more degenerate ($g_1/g_0 = 0.5$), the magnitude of specific heat is less than that of the equally degenerate case, and the maximum occurs at a higher temperature ($T \simeq 0.45\Delta/k_B$). In the presence of a magnetic field, the degenerate energy levels are lifted due to the Zeeman effect. In general, there are two sources of Schottky contributions to the specific heat. The degenerate energy levels of electron magnetic moment associated with J are split in the presence of the field. Also, the atomic nucleus spins has a magnetic moment, and the degenerate levels can be lifted by the field. A peak in specific heat associated with atomic nuclear can be observed at extremely low temperatures. The entropy associated with Schottky anomaly can be obtained by

$$S_{Sch} = \int_0^T dT \frac{C_{Sch}}{T}. \tag{1.10}$$

In general, extracting C_{Sch} from the specific heat is often difficult because it requires a subtraction of electronic and lattice contributions as well as other contributions such as phase transitions.

1.9 Transport Phenomena: DC Conductivity

Transport phenomena (e.g. electrical and thermal conductivity) in crystals is often described well by the semiclassical Boltzmann transport theory. The Drude model for the DC conduc-

tivity can be derived from the evolution of the distribution function in space, momentum, and time. The Boltzmann transport equation is given by

$$\underbrace{\frac{\partial g}{\partial t} + \vec{v} \cdot \frac{\partial g}{\partial \vec{r}} + \vec{F} \cdot \frac{1}{\hbar} \frac{\partial g}{\partial \vec{k}}}_{\text{"Drift terms"}} = \underbrace{\left.\frac{\partial g}{\partial t}\right|_{coll}}_{\text{"Collision terms"}} . \tag{1.11}$$

where $\vec{F}$ is the macroscopic forces such as temperature gradient, electric field, and magnetic field and g is the distribution function for electrons. If the system is perturbed by small external force, the system will move out of equilibrium, and collisions within the system will lead the system to relax back to equilibrium within a characteristic time. In the relaxation time approximation (RTA), the collision term will become

$$\left.\frac{\partial g}{\partial t}\right|_{coll} = -\frac{[g(\vec{k}) - g_0(\vec{k})]}{\tau(\vec{k})}, \tag{1.12}$$

where τ is the relaxation time and g and g_0 are distribution functions of perturbed and equilibrium state, respectively. Since the electrical conductivity is the linear response from a small applied electric field, the distribution function can be linearlized as

$$g = g_0 + g_1, \tag{1.13}$$

where g_0 is the distribution function in thermal equilibrium and g_1 is the deviation from the thermal equilibrium distribution. Substituting Eq. (1.13) and Eq. (1.12) into Eq. (1.11), the linearized Boltzmann equation can be obtained:

$$\frac{\partial g_1}{\partial t} + \vec{v} \cdot \frac{\partial g_0}{\partial \vec{r}} + \vec{F} \cdot \frac{1}{\hbar} \frac{\partial g_0}{\partial \vec{k}} = -\frac{g_1}{\tau}. \tag{1.14}$$

For DC conductivity, a uniform ($\frac{\partial g_0}{\partial \vec{r}} = 0$) and static field $\vec{E}$ ($\frac{\partial g_0}{\partial t} = 0$) at fixed temperature are considered. Using $\vec{F}(\vec{r}, \vec{k}) = -e\vec{E}$, the linearized distribution function can be obtained:

$$g = g_0 + \frac{e}{\hbar} \vec{E} \cdot \frac{\partial g_0}{\partial \vec{k}} \tag{1.15}$$

The current density can be obtained by integrating the velocity and the distribution of electrons in momentum space over the first Brillouin zone:

$$\vec{j}(\vec{r}, t) = -\frac{e}{4\pi^3} \int_{1^{st}BZ} v(\vec{k}) g(\vec{k}) d\vec{k} \tag{1.16}$$

By substituting the linearized distribution Eq. (1.15) into Eq. (1.16) and using $\partial g_0/\partial k_x = (\partial g_0/\partial \varepsilon)\hbar v_x$, the conductivity can be obtained since $j_x = \sigma E_x$:

$$\sigma = -\frac{e^2}{4\pi^3}\int d\vec{k} v_x^2(\vec{k})\tau(\vec{k})\frac{\partial g_0}{\partial \varepsilon} \tag{1.17}$$

By changing $d\vec{k}$ to energy $\vec{\varepsilon}$ and transforming to coordinates along the constant energy surface,

$$d\vec{k} = \frac{d\varepsilon dS_\varepsilon}{|\partial\varepsilon/\partial\vec{k}|} = \frac{d\varepsilon dS_\varepsilon}{\hbar|v(\vec{k})|}. \tag{1.18}$$

Using $-\frac{\partial g_0}{\partial \varepsilon} = \delta(\varepsilon - \varepsilon_F)$ since only electrons at the Fermi level contribute to the conduction, the conductivity can be expressed as:

$$\sigma = \frac{e^2}{4\pi^3\hbar}\int dS_\varepsilon d\varepsilon \frac{v_x^2(\vec{k})}{v(\vec{k})}\tau(\vec{k})\delta(\varepsilon - \varepsilon_F) \tag{1.19}$$

In general, $v(\vec{k})$ and $\tau(\vec{k})$ vary over Fermi surface, but an average value $\left\langle (v_x^2(\vec{k})/v(\vec{k}))\tau(\vec{k})\right\rangle_{\varepsilon_F}$ can be taken outside the integral. For nearly free electrons (i.e a Fermi sphere), this average is $\frac{1}{3}v(\varepsilon_F)\tau(\varepsilon_F)$, where ε_F is $\hbar^2k_F^2/2m^*$. Using $k_F^3 = 3\pi^2 n$, Eq. 1.19 reduces to

$$\sigma = \frac{e^2\tau(\varepsilon_F)n}{m^*}, \tag{1.20}$$

which is the Drude's equation for DC electrical conductivity.

1.10 Scattering Mechanism

The conductivity derived above is only valid when $T = 0$. The resistivity is defined as the reciprocal of the conductivity. For temperature dependence of resistivity, an ad-hoc temperature dependence in the relaxation time τ needs to be added to Eq. 1.20. Therefore, the total observed resistivity is the sum of resistivities due to the contributions of the various independent scattering mechanisms, which is described by the Matthiessen rule:

$$\begin{aligned}\rho = \frac{1}{\sigma} = \frac{m_e}{ne^2\tau_{total}} &= \frac{m_e}{ne^2}\left(\frac{1}{\tau_{el-imp}} + \frac{1}{\tau_{el-ph}} + \frac{1}{\tau_{el-el}} + ...\right) \\ &= \rho_{el-imp} + \rho_{el-ph} + \rho_{el-el} + ...,\end{aligned} \tag{1.21}$$

where ρ_{el-imp} is the resistivity due to electron-impurity scattering, ρ_{el-ph} is the resistivity due to electron-phonon scattering, and ρ_{el-el} is the resistivity due to electron-electron scattering.

Types of electron scattering due to impurities include lattice imperfections, boundaries, and impurity atoms. In general, the resistivity of a sample with impurities is always higher than that of a perfect sample, and the scattering rate due to non-magnetic impurities is

temperature independent. As $T \to 0$, the resistivity approaches to a finite value. This finite resistivity $\rho(T = 0)$ is known as the residual resistivity ρ_0. There are some cases where impurity atoms play a significant role in resistivity at low temperatures. When impurities are magnetic atoms with a spin degree of freedom, electrons near the Fermi energy scatter off the magnetic ions resonantly due to the coupling between the local spin from magnetic impurities and the spin from conduction electrons, and this energy dependent resonant scattering gives rise to temperature dependence of the resistivity at low temperatures. Upon cooling a metallic sample, the resistivity typically decreases, but below a characteristic temperature T_K, the resistivity rises again, exhibiting a minimum in the resistivity of the magnetically contaminated sample. This resonant scattering has the logarithmic temperature dependence, and this phenomena is observed in a material which exhibits the Kondo effect.

The resistivity in typical metals increases with increasing temperature. This is due to the scattering of electrons with the phonons, the collective excitations of the lattice vibration. At high temperatures ($T \gg \Theta_D$), all modes are excited, and the relaxation time τ_{el-ph} for electron-phonon scattering is proportional to the number of occupied phonon states, and the total number of phonons which contribute to the scattering is proportional to temperature. Thus, the resistivity due to electron-phonon scattering increases linearly with T. At low temperatures ($T \ll \Theta_D$), the number of phonons increases with T^3, and there is an additional T^2 contribution associated with the angle dependence of the scattering process, which gives rise to the T^5 dependence in resistivity due to electron-phonon scattering. Thus, the temperature dependence of resistivity due to electron-phonon scattering is given by

$$\rho(T) \propto \begin{cases} T^5, & T \ll \Theta_D \\ T, & T \gg \Theta_D. \end{cases} \tag{1.22}$$

The scattering mechanisms mentioned above are described by the free electron gas model which is based on the assumption that electrons are not interacting each other. At sufficient low temperatures, the interaction between electrons becomes dominant, and the electron-electron interactions need to be taken into account. According to Landau's Fermi Liquid (FL) theory, interacting electrons are treated as quasiparticles which scatter with themselves and have an intrinsic decay time. The average lifetime of a Fermi liquid quasiparticle is inversely proportional to the square of an energy required to excite an quasiparticle above the Fermi surface:

$$\tau(\epsilon) \propto \frac{1}{(\epsilon - \epsilon_F)^2}. \tag{1.23}$$

At temperatures $T \ll T_F$, the average energy required to excite the quasiparticle above the Fermi surface is $\epsilon = k_B T$. Thus, the average lifetime of the quasiparticle is proportional to $1/T^2$. Since resistivity is inversely proportional to lifetime, the temperature dependence of resistivity at low temperatures due to electron-electron interaction is quadratic in temper-

ature:

$$\rho_{el-el} \propto T^2. \tag{1.24}$$

Because the electron-electron interactions and the scattering with impurities are dominant at low temperatures $T \ll T_F$, the resistivity of a typical metal can be described by

$$\rho = \rho_0 + AT^2. \tag{1.25}$$

1.11 Heavy Fermion

The Heavy Fermion (HF) system is typically referred to as a collection of intermetallic compounds, especially Ce-, Yb-, or U-containing compounds, whose effective mass is much larger than the mass of a free electron. The value of effective mass can be obtained by specific heat measurement. In general, a compound with the γ value larger than 400 mJ/mol-K^2 are considered to be heavy fermion material.

Chapter 2

Thermodynamic and Transport Properties of Single Crystal $YbNi_4Cd$

2.1 Introduction

The studies of Ce- and Yb-based intermetallic compounds have been shown diverse ground states such as heavy fermion (HF) behavior, unconventional superconductivity, intermediate valence, non-Fermi liquid behavior in the proximity of the quantum critical point (QCP)[15, 16, 17, 18, 19].

The competition between the Kondo effect and the Ruderman- Kittel - Kasuya - Yosida (RKKY) exchange interaction often leads to unusual ground states and also plays the important role in our understanding of heavy fermion materials [20]. When the magnetic ions occupy on a network of tetrahedra in a face-centered cubic lattice with antiferromagnetic coupling, the frustration of antiferromagnetic interactions needs to be taken into account [21, 22, 23, 24]. In addition, a significant role in determining the thermodynamic and transport properties is expected from the crystalline electric field (CEF) effect.

Ytterbium-based ternary intermetallic compounds $YbCu_4X$ (X = Mg, Zn, Pd, Ag, Cd, In, Au, Tl) with a face-centered cubic structure exhibit a number of magnetic ground states [25]. The compounds with X = Ag, Cd, and Zn show a heavy fermion behavior without magnetic ordering, with the linear specific heat coefficient $\gamma \sim$200 mJ/mol-K^2 [26, 25]. The compounds with X = Pd and Au exhibit magnetic ordering below 1 K, in which their physical properties at low temperatures are dominated by the RKKY interaction and CEF effect [27]. Among these compounds, $YbCu_4In$ has been studied extensively due to its first order isostructural valence transition at T_v = 42 K [28, 29]. The low-carrier RCu_4In (R = Gd - Tm) system indicates a large frustration factor ($|\theta_p/T_N|$), implying the geometrical frustration of spins [30, 31].

In a continuing search for new Yb-based heavy fermion compounds, we have successfully grown single crystals of $YbNi_4Cd$ using Cd flux. Ternary RNi_4Cd (R = Ce - Lu, Y, and Sc)

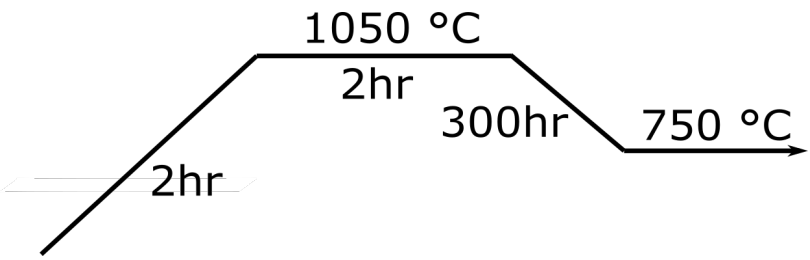

Figure 2.1: Temperature profile of single crystal $YbNi_4Cd$ growth.

compounds crystallize in the cubic $MgCu_4Sn$-type structure [32, 5], which have the same crystal structure as $YbCu_4X$. The lattice parameter of the RNi_4Cd intermetallics follows the lanthanoid contraction, where the lattice parameter decreases from Pr- to Lu-compound [5]. The magnetic Yb^{3+} state, inferred from the lanthanoid contraction, led us to investigate the thermodynamic and transport properties of $YbNi_4Cd$ single crystals.

2.2 Experimental Procedure

Raw elements of Yb, Ni, and Cd piece were cut into smaller pieces and placed in an alumina crucible in the ratio 1:4:30, and then sealed into an amorphous silica tube under partial Argon atmosphere. The ampoule was heated up to 1050 °C over two hours, held there for two hours, and then slowly cooled down to 750 °C over 300 hours. The temperature profile of the furnace for crystal growth is shown in Fig. 2.1. Right after the ampoule was removed from the furnace, the crystals were separated from the flux by a centrifuge. The surfaces of the crystals were polished to remove the excess flux prior to any measurements of its physical properties. A single crystal of $YbNi_4Cd$ with flux droplets adhered to its surfaces is shown in Fig. 2.2. For magnetization measurements, the dc magnetization as a function of temperature from 1.8 to 300 K, and magnetic field up to 70 kOe, was measured in a Quantum Design (QD) magnetic property measurement system (MPMS). For transport properties, four-probe ac resistivity measurements were performed from 300 K down to 0.4 K in a QD physical property measurement system (PPMS) with a 3He option. Specific heat was measured by the relaxation technique down to $T = 0.36$ K in a QD PPMS.

2.3 Experimental Results

2.3.1 Crystal Structure of $YbNi_4Cd$ and YNi_4Cd

To verify the phase and determine the lattice parameter, powder X-ray diffraction patterns were collected in a Rigaku MiniFlex diffractometer at room temperature. The single crystals were crushed into fine powder using a mortar and pestle, and mixed with Si-reference powder to calibrate the instrumental zero shift. The top and bottom panel in Fig. 2.3 show the XRD patterns of $YbNi_4Cd$ and YNi_4Cd, respectively. Whereas a small amount of cadmium phase

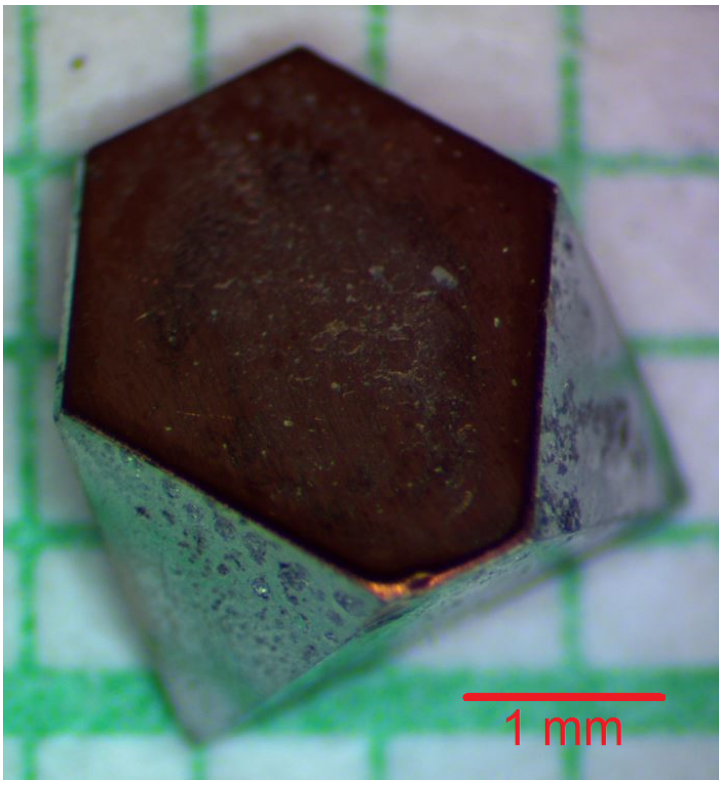

Figure 2.2: Single crystal of $YbNi_4Cd$ with unpolished surfaces.

is detected for $YbNi_4Cd$, as marked by a blue triangle, YNi_4Cd shows no impurity phase. The detected cadmium peaks are probably due to the flux inclusion inside the sample and/or droplets on the sample surface. All the peak positions are well indexed with a face-centered cubic $MgCu_4Sn$-type structure with space group $F\bar{4}3m$ and a lattice parameter $a = 6.975$ Å for R = Yb and $a = 7.031$ Å for R = Y. The obtained lattice parameters are consistent with an earlier report: 6.983 Å for R = Yb and 7.031 Å for R = Y [5].

2.3.2 Magnetic and Electronic Properties of YNi_4Cd

YNi_4Cd has magnetic and electronic properties consistent with a paramagnetic, intermetallic compound. The temperature-dependent magnetic susceptibility, $\chi(T) = M/H$, of YNi_4Cd at $H = 1$ kOe applied along [111] direction is shown in Fig. 2.4 (a). The magnetic susceptibility depends weakly on temperature down to 75 K, then starts to rise below 75 K, which is probably due to the presence of paramagnetic impurities. The magnetization isotherm at $T = 2$ K increases quasilinearly with increasing magnetic field up to 70 kOe as shown in Fig. 2.4 (b). The temperature-dependent specific heat, C_p, of YNi_4Cd is shown in Fig. 2.4 (c). The specific heat reaches the value of ∼150 J/mol-K at 300 K, which is close to the Dulong-petit limit and does not show any signature of a phase transition below 300 K. The electronic specific heat coefficient γ and the Debye temperature θ_D were ob-

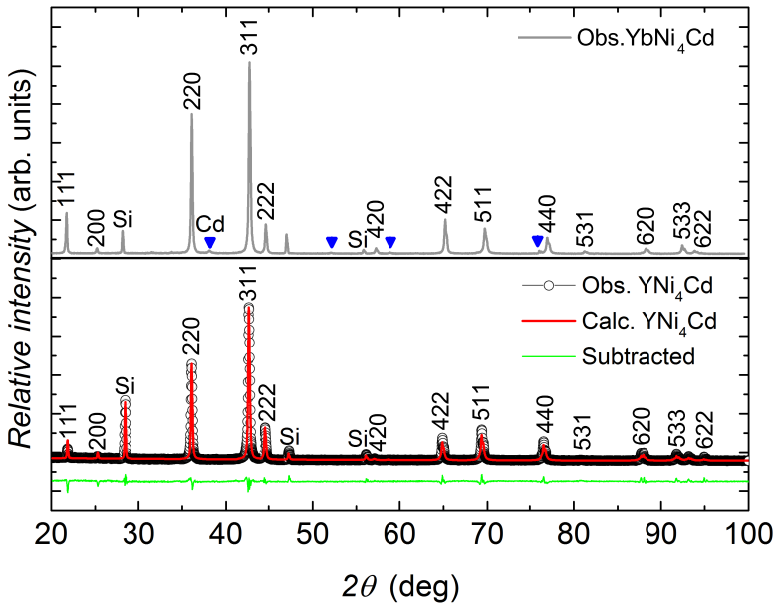

Figure 2.3: Powder X-ray diffraction patterns of $YbNi_4Cd$ (top) and YNi_4Cd (bottom). Blue triangles in top panel indicate impurity peaks assigned to Cd. In the bottom panel, the observed and calculated XRD patterns and their difference are shown in open circle, red line, and green line, respectively. Both $YbNi_4Cd$ and YNi_4Cd diffraction patterns include Si peaks, in which Si power is added intentionally to correct the zero shift of the diffractometer.

tained by taking into account only electronic and lattice contributions to the specific heat, $C_p(T) = \gamma T + \beta T^3$. These coefficients are extracted from the C_p/T versus T^2 plot as shown in the inset of Fig. 2.4 (c). The obtained γ and θ_D for YNi_4Cd are $\sim$14 mJ/mol-K^2 and $\sim$ 200 K, respectively. The temperature-dependent electrical resistivity, $\rho(T)$, of YNi_4Cd shown in Fig. 2.4 (d) clearly shows metallic behavior, with a linear decrease in resistivity with decreasing temperature. Below 50 K, the resistivity curve starts to saturate with a resistivity value of 2.92 $\mu\Omega$ cm at 1.8 K.

2.3.3 Magnetic Properties of $YbNi_4Cd$

The temperature-dependent inverse magnetic susceptibility, $1/\chi(T) = H/M$, of $YbNi_4Cd$ is shown in Fig. 2.5. No phase transition is detected down to 1.8 K. The magnetic susceptibility follows the Curie-Weiss law, $\chi(T) = C/(T - \theta_P)$ above 100 K, where C is the Curie constant and θ_P is the Weiss temperature. The effective magnetic moment estimated from the Curie constant is $\mu_{eff} = 4.81\ \mu_B$, which is somewhat higher than the theoretical effective magnetic moment of free Yb^{3+} ions (4.54 μ_B). The calculated Weiss temperature is $\theta_P = -16$ K, suggesting that the antiferromagnetic exchange interaction is dominant. The magnetic susceptibility deviates from the Curie-Weiss law below 100 K, which suggests that the degeneracy of the $J = 7/2$ of Yb^{3+} manifold is lifted by CEF effect.

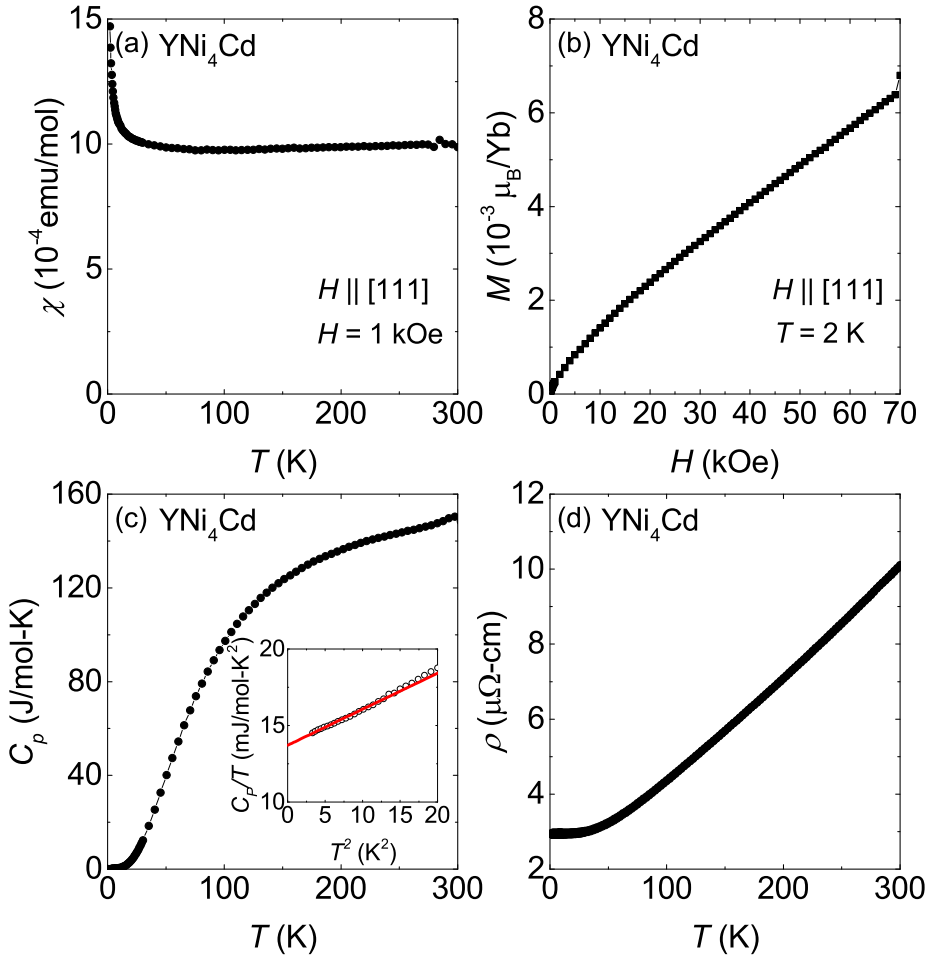

Figure 2.4: (a) Temperature-dependent magnetic susceptibility of YNi_4Cd at $H = 1$ kOe. (b) Magnetization isotherm of YNi_4Cd at $T = 2$ K. (c) Temperature-dependent specific heat of YNi_4Cd. Inset: The specific heat is shown as C_P/T vs T^2. The solid line is a fit to determine γ and θ_D. The fit is performed below 15 K^2. (d) Temperature-dependent electrical resistivity of YNi_4Cd.

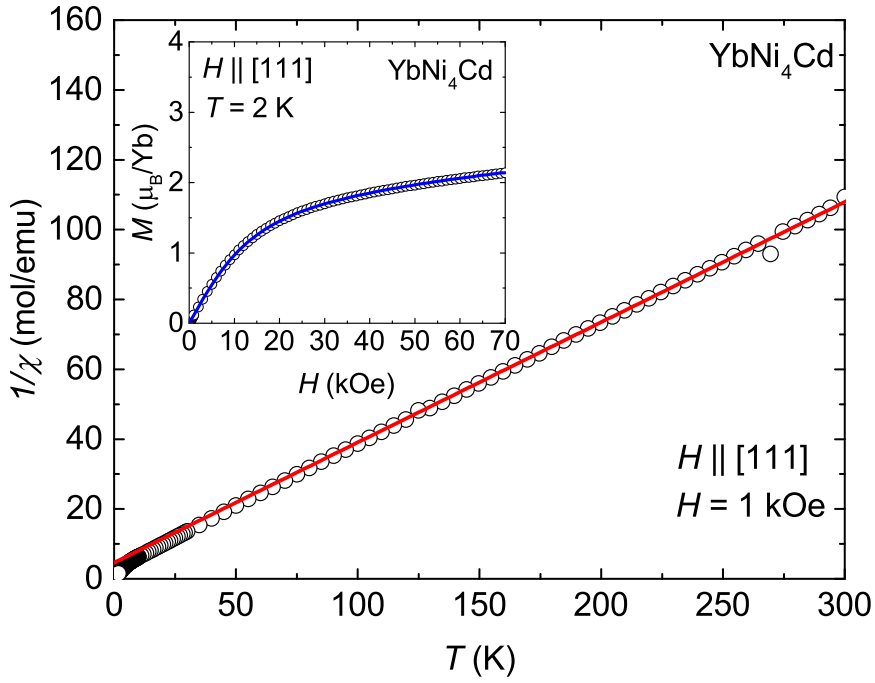

Figure 2.5: Inverse magnetic susceptibility of $YbNi_4Cd$ at $H = 1$ kOe applied along the [111] direction. Solid line represents Curie-Weiss fit. Inset shows magnetization isotherm of $YbNi_4Cd$ for both increasing (open circle) and decreasing (solid line) magnetic fields at $T = 2$ K.

The magnetization isotherm, $M(H)$, of $YbNi_4Cd$ at 2 K for $H \parallel [111]$ is shown in the inset of Fig. 2.5. No hysteresis is observed upon increasing and decreasing the field. The $M(H)$ curve follows a Brillouin-function-like behavior, reaches slightly above 2 μ_B/Yb at 70 kOe, which is the half of the theoretical saturated magnetization value $M_{sat} = g_J J$ (4 μ_B/Yb). This reduction in magnetization is possible evidence for CEF effects and Kondo screening.

2.3.4 Temperature-dependent Specific Heat of $YbNi_4Cd$ and $YbNi_4Cd$

The temperature-dependent specific heat, $C_p(T)$, of $YbNi_4Cd$ and the nonmagnetic isostructural analog YNi_4Cd are plotted in Fig. 2.6 (a). The $C_p(T)$ curve of $YbNi_4Cd$ shows a broad hump at ~20 K and a sharp pronounced peak at around ~0.97 K, which is typically ascribed to the transition from a paramagnetic state to a magnetically ordered state, as shown in Fig. 2.6 (b). In zero field, the estimated γ value of $YbNi_4Cd$ is ~26 mJ/mol-K^2 from the C_p/T versus T^2 plot as shown in Fig. 2.6 (c). The obtained Sommerfeld coefficient value of the magnetic $YbNi_4Cd$ compound is of the same order as in the nonmagnetic YNi_4Cd. The γ value can also be estimated by a linear extrapolation of the C_p/T curve below 0.4 K and estimated to be ~90 mJ/mol-K^2 as shown in Fig. 2.6 (d). It should be noted that because of the phase transition below 0.97 K and the broad feature around 20 K associated with

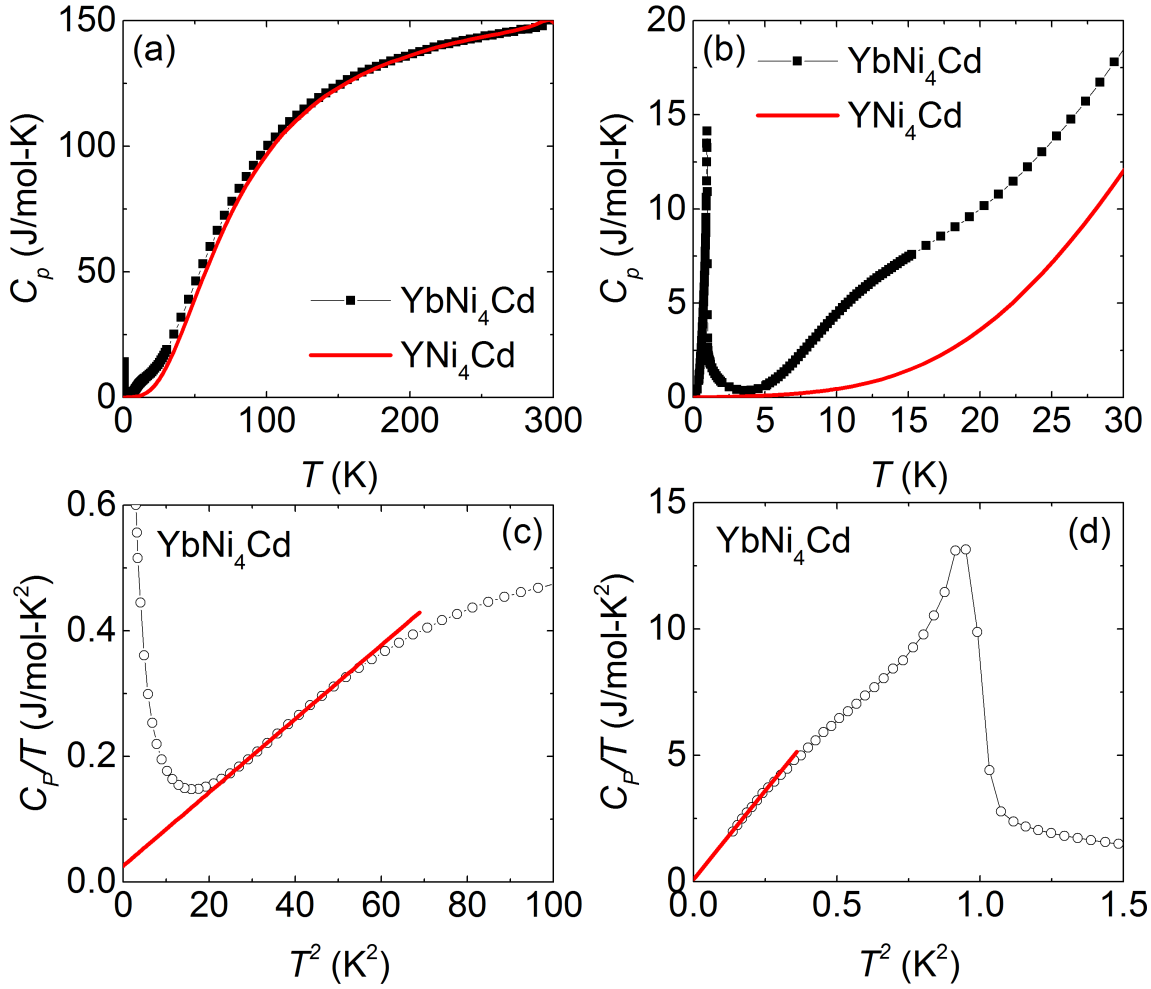

Figure 2.6: (a) $C_p(T)$ curves for RNi$_4$Cd (R = Yb and Y). (b) Expanded plot below 30 K. (c) C/T vs. T^2 plot for YbNi$_4$Cd. Solid line represents $C_p(T) = \gamma T + \beta T^3$ fit. (d) C/T vs. T^2 plot for YbNi$_4$Cd at low temperatures. Solid line is a linear extrapolation of the data below 0.5 K.

the CEF effect, the γ and Θ_D of YbNi$_4$Cd cannot be reliably obtained by using the relation $C_p(T) = \gamma T + \beta T^3$.

2.3.5 Temperature-dependent Magnetic Specific Heat of YbNi$_4$Cd

The magnetic contribution, C_m, in specific heat can be estimated by taking the difference between the specific heat of YbNi$_4$Cd and YNi$_4$Cd and is plotted in Fig. 2.7. The C_m curve shows a broad maximum centered at ∼30 K, indicating that there is a significant magnetic contribution from Yb^{3+} ions above the phase transition. The magnetic entropy is estimated by integrating C_m/T from the base temperature, $S_m = \int \frac{C_m}{T} dT$, and plotted in the inset of Fig. 2.7. Note that this will underestimate the total magnetic entropy, especially at low temperature. The S_m at the magnetic ordering temperature reaches about 70 % of Rln(2),

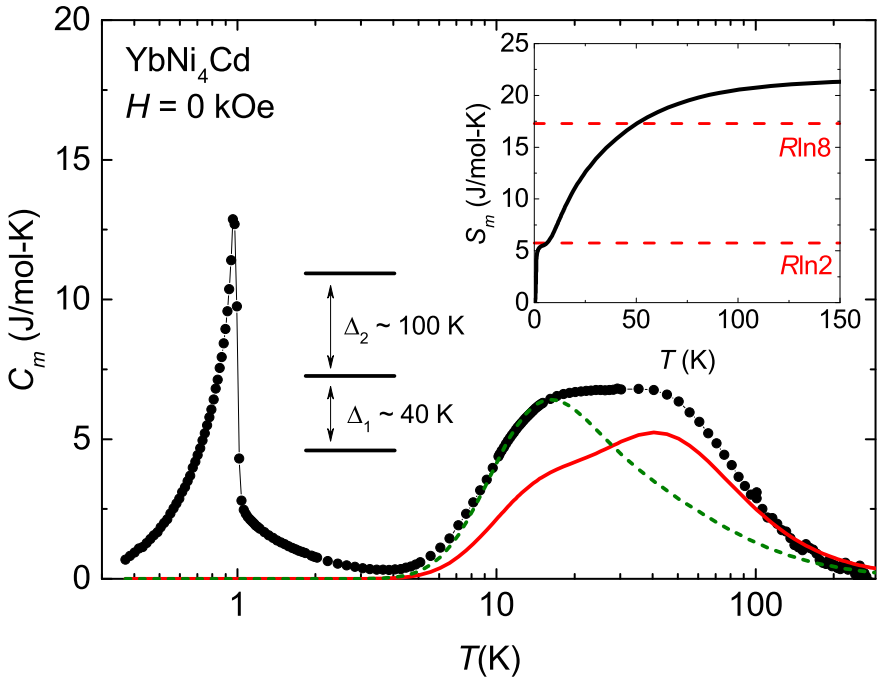

Figure 2.7: Temperature dependence of the C_m for $YbNi_4Cd$. Inset shows the magnetic entropy S_m. Dashed and solid lines represent Schottky contributions based on the 2-2-4 and 2-4-2 energy levels, respectively, with $\Delta_1 = 40$ K and $\Delta_2 = 100$ K.

suggesting that the sharp anomaly at 0.97 K in specific heat comes from the magnetic order in a doublet ground state. The full $R\ln(8)$ entropy for $J = 7/2$ is recovered at ∼50 K. The S_m curve saturates slightly higher than $R\ln(8)$, which we believe is due to subtraction error. The pronounced anomaly around 30 K in C_m can be associated with an electronic Schottky contribution involving three CEF split levels, as expected for Yb^{3+} in a cubic crystal symmetry.

For cubic symmetry, the $J = 7/2$ multiplets can be split into either a doublet-quartet-doublet (2-4-2) or a doublet-doublet-quartet (2-2-4)[33]. The C_m in the paramagnetic state is analyzed in terms of a Schottky anomaly by considering these two energy level schemes, and the resulting fits are shown in Fig. 2.7. Due to the subtraction error (mostly the lattice contribution), the overall analysis is rather qualitative. A qualitative agreement with the experimental data is obtained for both 2-4-2 (solid line) and 2-2-4 (dashed line) energy level schemes with $\Delta_1 \sim 40$ K and $\Delta_2 \sim 100$ K. To observe the crystal field excitations directly, neutron scattering experiments would be necessary. Although the fits only reproduce the shape of the anomaly in C_m, it is clear that the ground state doublet is well separated from the first excited state.

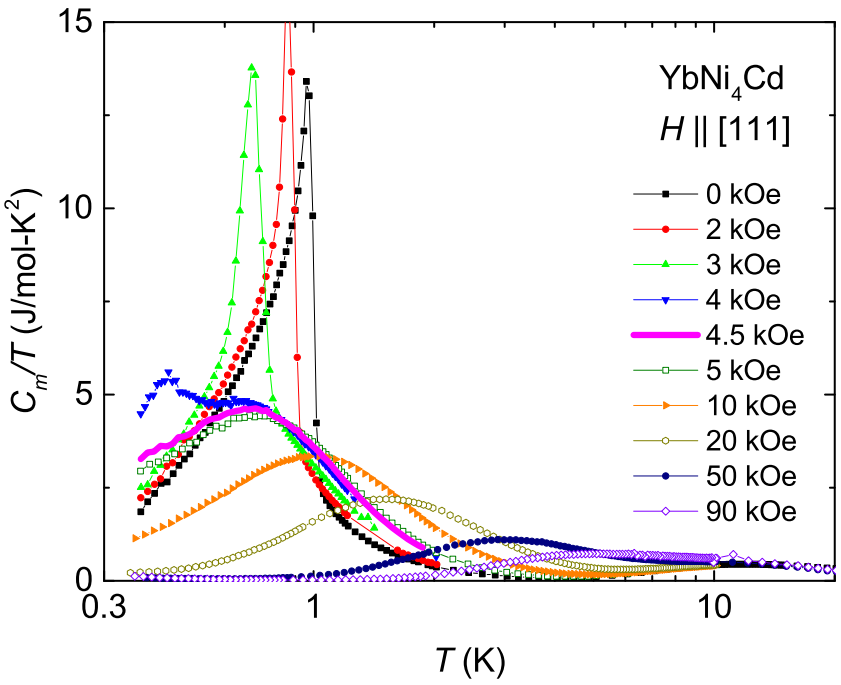

Figure 2.8: Curves of C_m/T vs. T for $YbNi_4Cd$ in various magnetic fields.

2.3.6 Magnetic Field-dependent Specific Heat of $YbNi_4Cd$

In order to examine the effect of an applied magnetic field on the magnetic ordering, the specific heat was measured up to 90 kOe for $H \parallel [111]$. The C_m curves for selected magnetic fields are plotted in Fig. 2.8 as C_m/T vs. $\log(T)$. A shift of the magnetic ordering temperature to lower temperatures is clearly seen for $H \leq 4$ kOe. For $H = 4.5$ kOe, the sharp peak in C_m/T curve is no longer visible, indicating that the phase transition is suppressed below 0.4 K. At this field, the C_m/T curve exhibits a broad maximum centered ~0.7 K. At higher fields, this peak broadens further and moves to higher temperatures, indicating that the magnetic entropy is removed at higher temperatures for larger applied fields. Such behavior has been found in Kondo lattice systems under magnetic fields and can be explained within the Kondo resonance-level model combined with CEF effect [34]. Note that C_m/T in the proximity of the critical field $H_c \sim 4.5$ kOe displays no clear indication of non-Fermi liquid behavior such as -$\log(T)$ dependence [17, 19].

2.3.7 Magnetic Field-dependent Magnetic Specific Heat of $YbNi_4Cd$

The magnetic field dependence of C_m at $T = 0.4$ K is shown in Fig. 2.9. The C_m/T shows a sharp peak as the magnetic field passes through the phase boundary. The peak shape is sharpened as temperature increases (see inset). Although the electronic specific heat coefficient (given by $\gamma = C_m/T$ for $T \to 0$) is not well-specified by the data, the C_m/T

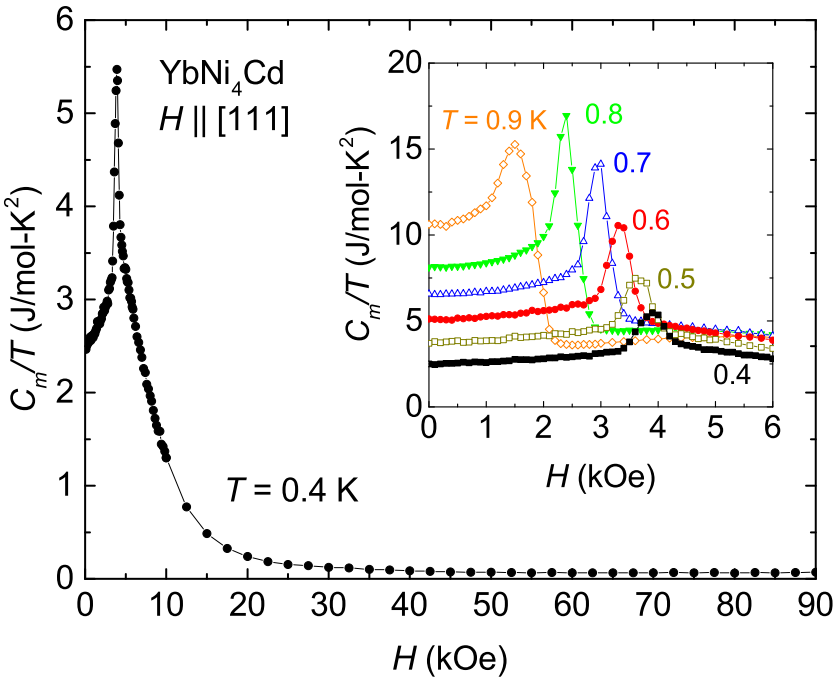

Figure 2.9: C_m/T vs. H for $YbNi_4Cd$ at $T = 0.4$ K. Inset shows C_m/T curves at selected temperatures plotted as a function of field.

curve at $T = 0.4$ K provides an estimate of the magnetic field dependence of γ. In the paramagnetic state, the C_m/T value drops from $\sim$3 J/mol-K^2 at 5 kOe to $\sim$0.07 J/mol-K^2 at 90 kOe, implying that the hybridization between $4f$ and conduction electrons in $YbNi_4Cd$ can be destroyed by external magnetic fields. It should be noted that the enhanced value of C_m/T at low temperatures is mainly associated with electronic Schottky contributions.

2.3.8 Temperature-dependent Resistivity of $YbNi_4Cd$

The temperature dependence of the electrical resistivity, $\rho(T)$, of $YbNi_4Cd$ is shown in Fig. 2.10. Electrical resistivity measurements show a behavior typical of Yb-based Kondo lattice compounds. In zero field, $\rho(T)$ shows two broad features at $\sim$2 and 25 K; the lower one is primarily related to Kondo scattering, while the higher one is primarily associated with the thermal population of CEF levels. The inset of Fig. 2.10 shows the $\rho(T)$ curves at various magnetic fields for $H \parallel [111]$. The magnetic transition in zero field manifests itself as a precipitous drop in $\rho(T)$ below 0.97 K. As magnetic field increases, a gradual suppression of the magnetic order is observed in $\rho(T)$. In the vicinity of the critical field, Fermi liquid behavior [$\rho(T) \propto T^2$] is found over a limited range of temperature and field. At very low temperatures and high fields, the $\rho(T)$ curves become flat, revealing an anomalous T^n dependence with $n > 2$.

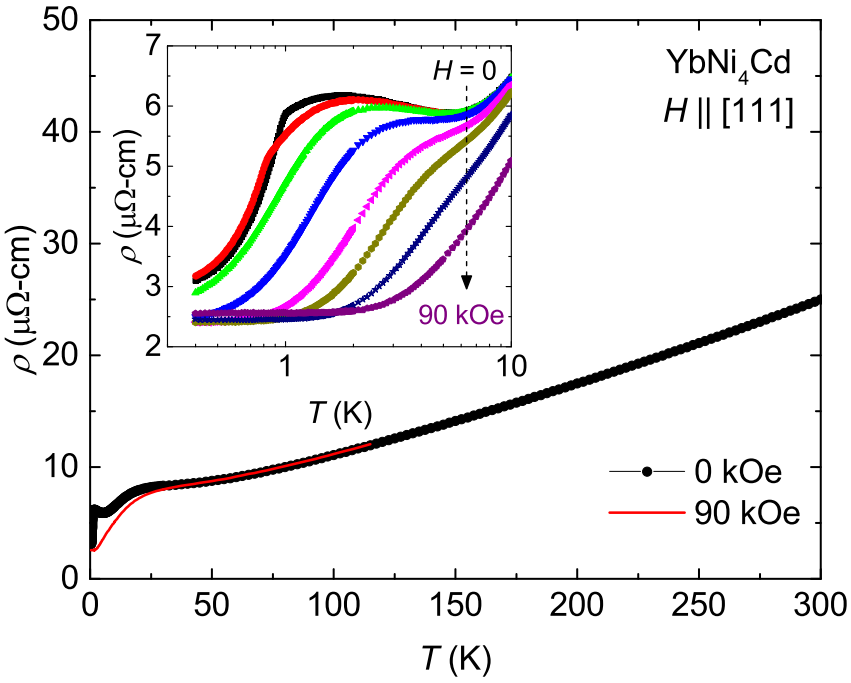

Figure 2.10: Temperature dependence of the electrical resistivity $\rho(T)$ for $YbNi_4Cd$ at $H = 0$ and 90 kOe. Inset shows $\rho(T)$ at selected magnetic fields $H = 0$, 2.5, 5, 10, 20, 30, 50, 90 kOe (from top to bottom).

2.3.9 Magnetic Field-dependent Resistivity of $YbNi_4Cd$

The magnetic field dependence of electrical resistivity, $\rho(H)$, elucidates some of features observed in $\rho(T)$. Figure 2.11 shows $\rho(H)$ curves for $H \parallel [111]$ below 10 K. $\rho(H)$ curves below 1 K exhibit a peak at the phase boundary, whereas $\rho(H)$ curves above 1 K vary monotonically. In the paramagnetic state ($H > 4$ kOe) $\rho(H)$ at 0.4 K shows a minimum around 15 kOe and linearly increases above 20 kOe as magnetic field increases. Note that $\rho(H)$ measurements indicate no hysteresis down to 0.4 K.

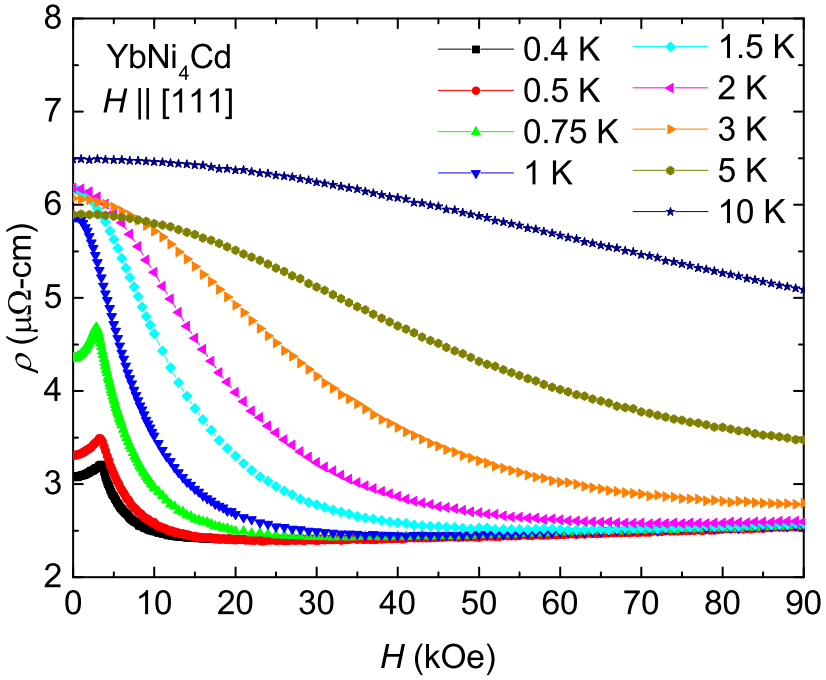

Figure 2.11: Magnetic field-dependent resistivity of $YbNi_4Cd$ at various temperatures.

Chapter 3

Discussion

3.1 Phase Diagram of $YbNi_4Cd$

The H - T phase diagram constructed from specific heat and resistivity measurements is plotted in Fig. 3.1. The critical temperature determined from temperature sweep is in good agreement with the critical field determined from field sweeps. As presented in the phase diagram, the magnetic ordering shifts towards lower temperature when magnetic field increases. The antiferromagnetic (AFM) ordering at $T_N = 0.97$ K is inferred from the lack of hysteresis in the electrical resistivity and specific heat measurements as well as the fact that the magnetic phase transition can be suppressed below 0.4 K by an applied magnetic field of 4 kOe.

3.2 Anomalous Electrical Resistivity of $YbNi_4Cd$

At low temperatures it is expected that for metallic systems, Fermi liquid (FL) behavior should be recovered in the paramagnetic (PM) state ($H > H_c$). Figures 3.2 (a), 3.2 (b), and 3.2 (c) show the resistivity curves of $YbNi_4Cd$ varying as $\rho(T) = \rho_0 + AT^n$ with $n \geq 2$ at low temperatures. In the vicinity of the AFM to PM phase boundary ($H = 5$ kOe), a T^n dependence with $n \approx 2$ in $\rho(T)$ is observed. For $H > H_c$, $\rho(T)$ displays an anomalous T^n dependence with $n > 2$, indicative of deviation from FL behavior. This suggests that an additional scattering mechanism in $\rho(T)$ needs to be considered. The exponent n gradually increases as magnetic field increases from 5 kOe and eventually reaches $n \simeq 4$ for $H > \sim$40 kOe as shown in Fig. 3.2 (d). The coefficient $A_n = (\rho(T) - \rho_0)/T^n$ and the residual resistivity value ρ_0, corresponding to each n, are plotted in Fig. 3.2 (e) and 3.2 (f), respectively. The A_n value quickly drops with increasing magnetic field for $H > H_c$. While the ρ_0 values above $\sim$20 kOe follow the resistivity curve at $T = 0.4$ K, the ρ_0 values below 20 kOe deviate from the resistivity curve at $T = 0.4$ K as shown in Fig. 3.2 (f). Note that the anomalous exponent with $n > 2$ has been observed in the fully saturated paramagnetic state for $CeAuSb_2$ [35], $YbNiSi_3$ [36], and $CeNiGe_3$ [37]. Pronounced non-Fermi

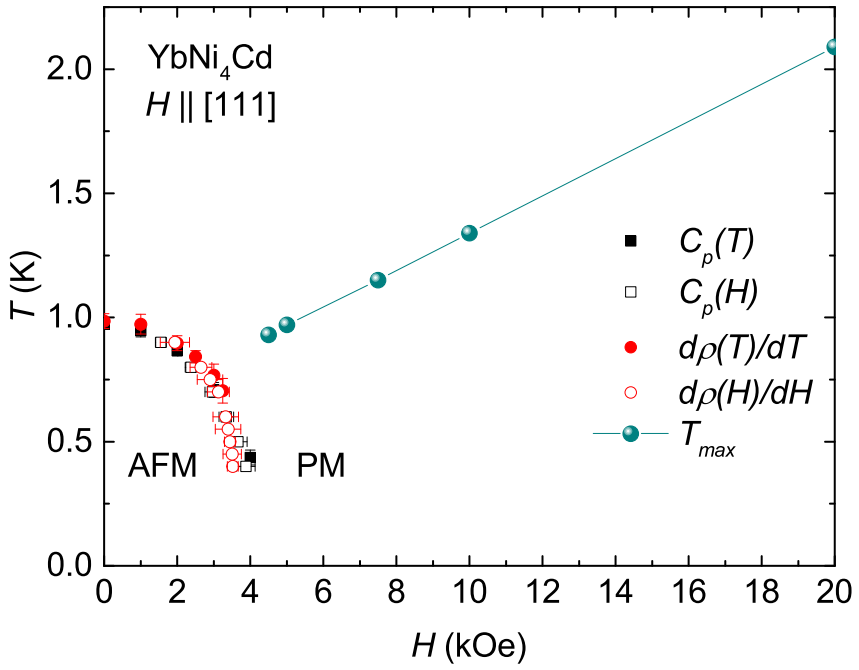

Figure 3.1: H-T phase diagram for $YbNi_4Cd$. The phase transitions are extracted from $C_p(T)$, $C_p(H)$, $d\rho(T)/dT$, and $d\rho(H)/dH$. T_{max} indicates a local maximum in $C_m(T)$ curves.

liquid (nFL) behavior ($\Delta\rho = AT^n$ with $n < 2$) is observed in the vicinity of the magnetic field tuned quantum critical point in HF AFM systems such as $YbRh_2Si_2$ [38, 39], $CeAuSb_2$ [35], YbAgGe [40], and YbPtBi [41]. However, for $YbNi_4Cd$, there is no clear indication of nFL behavior down to 0.4 K in the vicinity of H_c. In order to address the existence of nFL behavior, it is necessary to measure the resistivity below 0.4 K.

3.3 Electronic Schottky Contribution to Magnetic Specific Heat of $YbNi_4Cd$

In zero field, the specific heat shows that the AFM order develops from Yb^{3+} moments in a doublet ground state that is well separated from the first excited state. The rapid recovery of the $R\ln(2)$ ground state entropy at T_N, $S_m(T_N) = 0.7\ R\ln(2)$, suggests that the Kondo screening of the Yb^{3+} moments may play little role in $YbNi_4Cd$. In many HF antiferromagnets, despite the presence of a large ordered moment, one finds a small entropy release at T_N due to strong entanglement between $4f$- and conduction electrons. Thus, it is expected that the $4f$-electrons in $YbNi_4Cd$ compound are spatially well localized and weakly coupled to the conduction electrons. To explain the large value of C_m/T at low temperatures, it is necessary to consider multiple contributions. In the PM state, for $H > 4$ kOe, a broad peak is developed in C_m, which is the origin of the large C_m/T at low temperatures. The

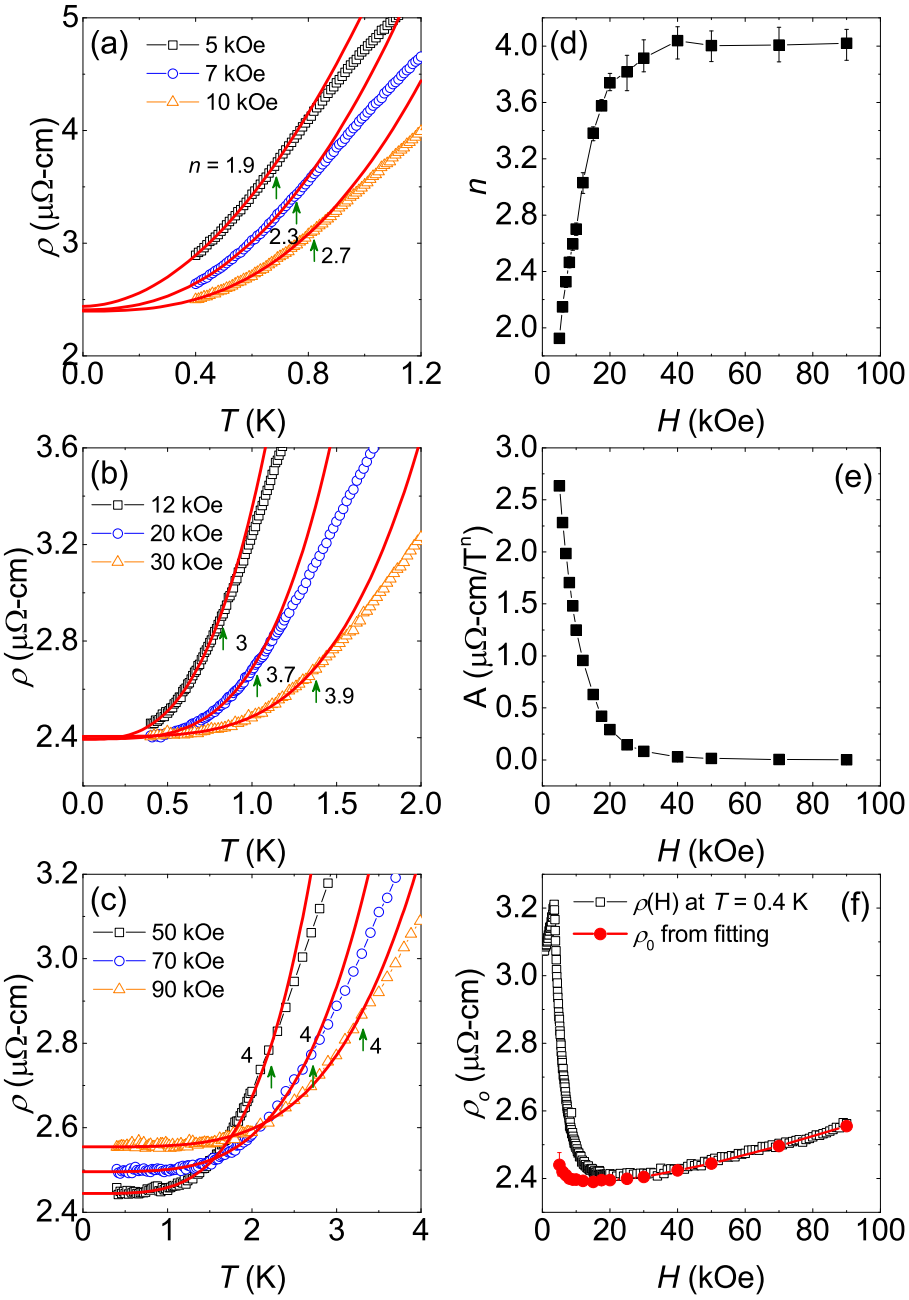

Figure 3.2: (a) $\rho(T)$ curves at $H = 5$, 7, and 10 kOe. (b) $\rho(T)$ curves at $H = 12$, 20, and 30 kOe. (c) $\rho(T)$ curves at $H = 50$, 70, and 90 kOe. Solid lines in (a), (b), and (c) represent the fit with $\rho(T) = \rho_0 + AT^n$. The fitting parameters n, A, and ρ_0 are plotted in (d), (e), and (f), respectively. The $\rho(H)$ curve at $T = 0.4$ K is plotted in (f)

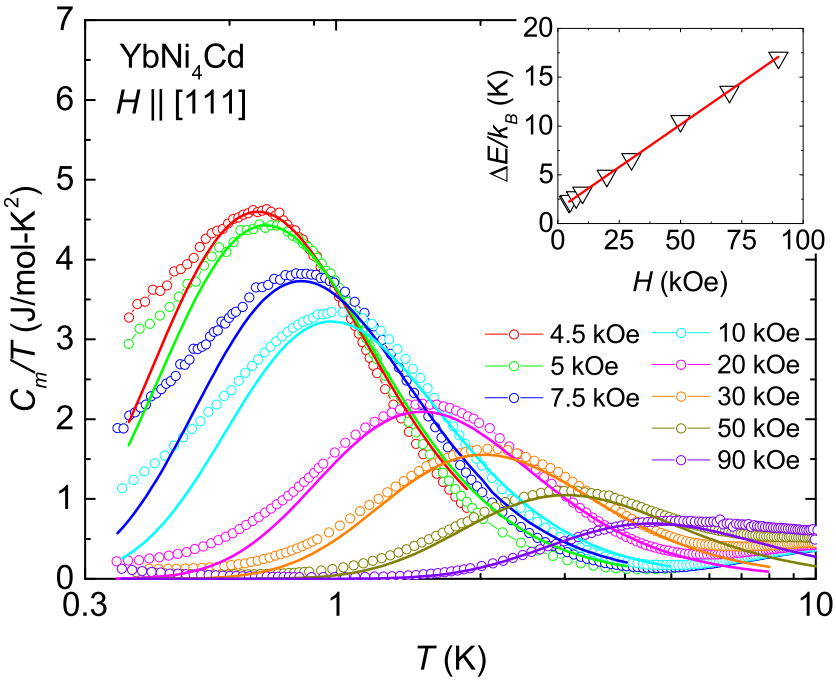

Figure 3.3: C_m/T curves at selected magnetic fields. Solid curves represent the electronic Schottky contribution. Inset shows the Δ as a function of field. Solid line is guided to the eye.

broad peak moves to higher temperatures with increasing magnetic field as we expect for an electronic Schottky contribution, C_{Sch}, to the specific heat due to the Zeeman effect. The Schottky contribution on the ground state doublet is shown in Fig. 3.3. The fit curves for C_{Sch} are obtained by only considering the splitting of the ground state doublet, where two levels are equally degenerated and separated by a gap Δ. The field dependence of Δ is plotted in the inset of Fig. 3.3. The maximum temperature, T_{max}, of the broad peak in C_m is shown in Fig. 3.3 (phase diagram). As expected, Δ increases linearly with magnetic field, which confirms that is indeed a Schottky anomaly. Therefore, the CEF splitting via Zeeman effect plays a crucial role in understanding the magnetic field dependence of thermodynamic and transport properties observed in the $YbNi_4Cd$. It should be noted here that the C_p curves show an upturn below $\sim$0.5 K for $H = 70$ kOe and below $\sim$0.7 K for $H = 90$ kOe, which is probably due to the nuclear Schottky contribution. Because the upturn shows only limited temperature range, we were not able to reliably subtract the nuclear contribution.

3.4 Anomalous Electronic Contribution and Possible Origins

On the other hand, there is a large difference ($\sim$1 J/mol-K^2) at $T = 0.4$ K for $H = 5$ kOe between C_m and the electronic Schottky contribution, indicating that the additional contributions much be considered. In order to obtain insight into the electronic contribution,

we assumed $C_m = \gamma T + C_{Sch}$ and γ was estimated by subtracting the electronic Schottky contribution. The $(C_m - C_{Sch})/T$ curves are plotted in the inset of Fig. 3.4. As can be seen from the figure, whereas $(C_m - C_{Sch})/T$ curves for $H_c < H < \sim$10 kOe continuously increase below the T_{max}, the curves for $H >\sim$30 kOe are almost temperature independent. Note that the $(C_m - C_{Sch})/T$ value around the critical field is much larger than the zero field γ value ($\gamma \sim$ 90 mJ/mol-K^2). Another convenient way of demonstrating the behavior of $(C_m - C_{Sch})/T$ is to plot the values at the lowest measured temperature as a function of magnetic field (Fig. 3.4). It can be clearly seen that the $(C_m - C_{Sch})/T$ at $T = 0.4$ K is quickly suppressed by applied magnetic fields and becomes almost field independent for $H > 30$ kOe. This behavior is also consistent with the $\rho(H)$ curve at $T = 0.4$ K, where the $\rho(H)$ slope changes from negative to positive around 20 kOe, and increases linearly up to 90 kOe. It should be noted that the $(C_m - C_{Sch})/T$ curves indicate a divergent behavior close to the H_c. To confirm any divergence of γ [for example, $-\log(T)$ or power law divergence] it is necessary to measure specific heat below 0.4 K.

One possible explanation for the low temperature behavior of $(C_m - C_{Sch})/T$ is that it originates from the Kondo contribution. This would be consistent with a large negative Weiss temperature ($\theta_p \sim$ -16 K) determined from the magnetic susceptibility. The magnetic field dependence of $(C_m - C_{Sch})/T$ is typical for HF systems, where it originates from the fact that the external magnetic field gradually destroys the Kondo effect. However, the absolute value ($\sim$ 1 J/mol-K^2) and the temperature dependence [$-\log(T)$ below T_{max}] of $(C_m - C_{Sch})/T$ curves close to the critical field cannot be solely explained by the Kondo effect. For a Kondo lattice system, the Kondo temperature T_K can be estimated by $T_K = Wj\pi R/3\gamma$ [16], where W is the Wilson number, j is the total angular momentum, and R is the gas constant. In zero field, the estimated T_K is $\sim$60 K for $j = 1/2$ and $\gamma = 0.09$ J/mol-K^2. The Kondo temperature can also be estimated from the magnetic susceptibility as $T_K \simeq |\theta_p|/4$ [16]. The θ_p value hints at the presence of Kondo interactions with a characteristic energy scale of about 16 K ($T_K < 16$ K). Note that this value of T_K is not in good agreement with that estimated from the specific heat. At H_c, the T_K is estimated to be $\sim$5 K for $j = 1/2$ with $\gamma \sim 1.1$ J/mol-K^2 at 0.4 K. Since the $(C_m - C_{Sch})/T$ continues to rise below 0.4 K, the T_K is expected to be smaller than 5 K. This is remarkable, since the Kondo temperature at H_c is well below the zero field value. We do no believe that this large enhancement of γ at H_c (which decreases the Kondo temperature) could be caused by such a small external magnetic field ($\sim$5 KOe). Therefore, we consider the possibility that antiferromagnetic short-range correlations may produce a large γ value. The instability to magnetism due to the short-range correlations has been shown in paramagnetic HF Kondo lattice compounds close to a quantum critical point [17, 19, 42, 43]. In this case, the AFM fluctuations can be coexist with Kondo fluctuations and the enhanced value of $(C_m - C_{Sch})/T$ observed for $YbNi_4Cd$ at low temperatures would reflect a combination of Kondo and AFM fluctuations. With increasing magnetic field the crossover between ordered state and paramagnetic state is evident at

$H = H_c$, however the resistivity and specific heat data down to 0.4 K do not confirm explicitly the presence of a QCP via non-Fermi-Liquid behavior. Therefore, although the AFM order can be suppressed by an external magnetic field, a classical QCP is not observed in $YbNi_4Cd$. This may indicate a weak hybridization between $4f$ and conduction electrons.

The lack of non-Fermi-liquid behavior is an indication that the observed low temperature properties are not related to a classical QCP. If the temperature dependence and the large value of $(C_m - C_{Sch})/T$ curves close to the critical field are not induced by the coupling of $4f$ local moments to the conduction electrons, they must be explained by another type of fluctuations. In a Kondo lattice system, quantum fluctuations can also be induced by the $4f$ local moments on their own, where the fluctuations can be tuned by varying the degree of magnetic frustration or tunning the dimensionality [44, 45]. In $YbNi_4Cd$, the antiferromagnetically coupled Yb^{3+} ions on the tetrahedra will be magnetically frustrated. The frustration parameter $|\theta_p/T_N| \sim 16$ observed for $YbNi_4Cd$ is sufficiently large to allow us to infer that the frustration may dominate the magnetic properties. Similar behavior has been observed in the related RCu_4In (R = rare-earth) compounds. Although the low carrier density RCu_4In compounds order antiferromagnetically, they exhibits a large frustration parameter as a signature of geometrical frustration [30, 31]. Since a large portion of the $R\ln(2)$ entropy is recovered at T_N, partial frustration, as suggested for the $GdCu_4In$ compound [23], may need to be considered for $YbNi_4Cd$. In general, the Kondo effect, delocalizing the magnetic $4f$-electrons to the Fermi level, is not beneficial for the formation of a frustrated state. The frustration parameter defined fundamentally for an insulating system is also no longer useful in metallic compounds, where the long-range RKKY interaction mediated by conduction electrons become dominant. It has been proposed, however, that the $4f$-electrons can be decoupled from the conduction electrons for sufficiently large frustration in the Kondo lattice system [46, 47]. Therefore, to explain the low temperature thermodynamic and transport properties the effect of (partial) magnetic frustration in $YbNi_4Cd$ should not be excluded from consideration. We suggest that the delicate balance among competing energy scales of both short-range and long-range interactions plays a crucial role for its low temperature phase. More detailed investigations of low temperature physical properties are needed to clarify the ground state of $YbNi_4Cd$.

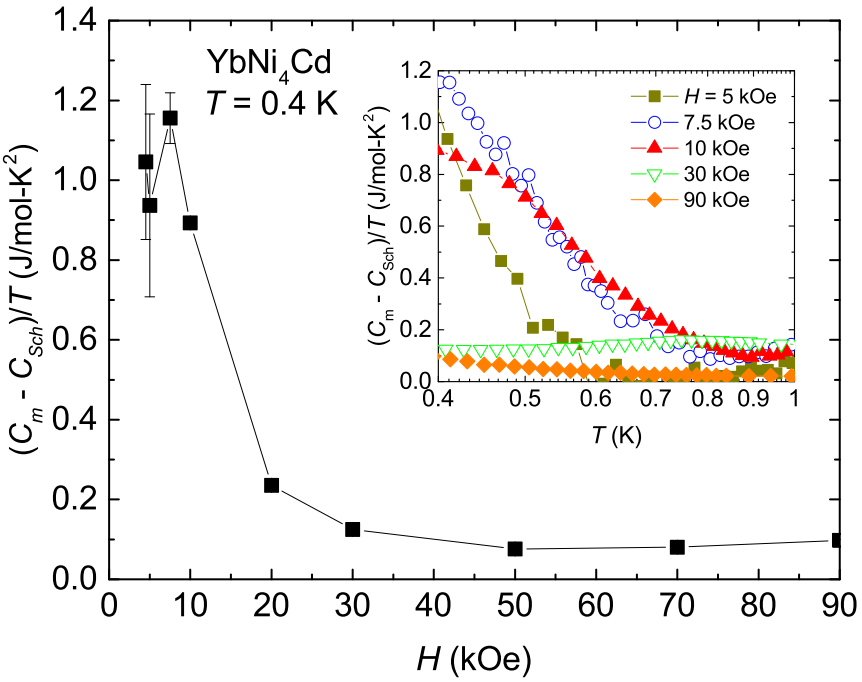

Figure 3.4: $(C_m - C_{Sch})/T$ at $T = 0.4$ K plotted as a function of field. Inset shows $(C_m - C_{Sch})/T$ curves at selected magnetic fields.

Chapter 4

Conclusion and Future Work

We have successfully grown the single crystals of $YbNi_4Cd$ and YNi_4Cd, which crystallize in the cubic $MgCu_4Sn$-type structure. The obtained experimental data show that $YbNi_4Cd$ is an antiferromagnetic Kondo lattice with strong crystalline electric field effect. The magnetic susceptibility measurement indicates that the Yb^{3+} moments occupying the tetrahedra are well localized. In zero field, the specific heat and resistivity measurements confirm that the $YbNi_4Cd$ compound undergoes an antiferromagnetic transition at $T = 0.97$ K. The low temperature behavior of specific heat and resistivity is strongly dependent on the strength of the magnetic field. An $H - T$ phase diagram has been constructed based on these measurements. Upon applying a magnetic field along the [111] direction, the magnetic phase transition can be suppressed below 0.4 K for $H > 4$ kOe. In the vicinity of the antiferromagnetic to paramagnetic phase boundary, no clear indication of non-Fermi-liquid behavior was observed. At higher fields an anomalous temperature dependence of the electrical resistivity was observed. Thermodynamic and transport measurements below 0.4 K are desirable in order to further clarify the ground state of $YbNi_4Cd$. In particular, it is critical to measure the specific heat to identify the origin of the large electronic specific heat coefficient close to the critical field.

Bibliography

[1] V. K. Pecharsky and Karl A. Gschneidner Jr. Giant magnetocaloric effect in $Gd_5(Si_2Ge_2)$. *Phys. Rev. Lett.*, 78(23):4494, 1997.

[2] F. Steglich, J. Aarts, C. D. Bredl, W. Lieke, D. Meschede, W. Franz, and H. Schäfer. Superconductivity in the Presence of Strong Pauli Paramagnetism: $CeCu_2Si_2$. *Phys. Rev. Lett.*, 43(25):1892, 1979.

[3] G. Giovannetti, S. Kumar, D. Khomskii, S. Picozzi, and J. van den Brink. Multiferroicity in Rare-Earth Nickelates $RNiO_3$. *Phys. Rev. Lett.*, 103(15):156401, 2009.

[4] G. R. Stewart, Z. Fisk, and M. S. Wire. New Ce heavy-fermion system: $CeCu_6$. *Phys. Rev. B*, 30(1):482, 1984.

[5] F. Tappe, C. Schwickert, and R. Pöttgen. Ternary ordered Laves phases $RENi_4Cd$. *Intermetallics*, 24:33–37, 2012.

[6] J. Lee, H. Park, N.R. Lee-Hone, D.M. Broun, and E. Mun. Thermodynamic and transport properties of $YbNi_4Cd$. *Phys. Rev. B*, 97(19):195144, 2018.

[7] F. Greuter and G. Blatter. Electrical properties of grain boundaries in polycrystalline compound semiconductors. *Semicond. Sci. Tech.*, 5(2):111, 1990.

[8] D. Souptel. Crystal growth and perfection of selected intermetallic and oxide compounds. *Dissertation, TU Dresden*, 2004.

[9] M. Tachibana. Beginner's Guide to Flux Crystal Growth. *Springer Japan*, 2017.

[10] P. C. Canfield and Z. Fisk. Growth of single crystals from metallic fluxes. *Philos. Mag. B*, 65(6):1117–1123, 1992.

[11] P. C. Canfield and I. R. Fisher. High-temperature solution growth of intermetallic single crystals and quasicrystals. *J. Cryst. Growth*, 225(2-4):155–161, 2001.

[12] C. Hammond. The Basics of Crystallography and Diffraction. *Oxford*, 214, 2001.

[13] Y. Waseda, E. Matsubara, and K. Shinoda. X-ray diffraction crystallography: introduction, examples and solved problems. *Springer Science & Business Media*, 2011.

[14] M. Bouvier, P. Lethuillier, and D. Schmitt. Specific heat in some gadolinium compounds. I. Experimental. *Phys. Rev. B*, 43(16):13137–13144, 1991.

[15] G. R. Stewart. Heavy-fermion systems. *Rev. Mod. Phys.*, 56:755–787, Oct 1984.

[16] A. C. Hewson. The Kondo problem to heavy fermions. *Cambridge University Press*, 2, 1997.

[17] G. R. Stewart. Non-Fermi-liquid behavior in d- and f-electron metals. *Rev. Mod. Phys.*, 73(4):797, 2001.

[18] G. R. Stewart. Addendum: Non-Fermi-liquid behavior in d- and f-electron metals. *Rev. Mod. Phys.*, 78(3):743, 2006.

[19] P. Gegenwart, Q. Si, and F. Steglich. Quantum criticality in heavy-fermion metals. *Nat. Phys.*, 4(3):186, 2008.

[20] S. Doniach. The Kondo lattice and weak antiferromagnetism. *Physica B+C*, 91:231–234, 1977.

[21] J. S. Smart. Effective field theories of magnetism. *Saunders*, (2), 1966.

[22] S. T. Bramwell and M. J. P. Gingras. Spin ice state in frustrated magnetic pyrochlore materials. *Science*, 294(5546):1495–1501, 2001.

[23] H. Nakamura, N. Kim, M. Shiga, R. Kmiec, K. Tomala, E. Ressouche, J. P. Sanchez, and B. Malaman. The partially disordered state of the frustrated face-centred cubic antiferromagnet. *J. Phys. Condens. Matter*, 11(4):1095, 1999.

[24] L. Balents. Spin liquids in frustrated magnets. *Nature*, 464(7286):199, 2010.

[25] J. L. Sarrao, C. D. Immer, Z. Fisk, and C. H. Booth. Physical properties of $YbXCu_4$ (X= Ag, Au, Cd, Mg, Tl, and Zn) compounds. *Phys. Rev. B*, 59:6855–6866, 1999.

[26] T. Graf, J. M. Lawrence, M. l. F. Hundley, J. D. Thompson, A. Lacerda, E. Haanappel, M. S. Torikachvili, Z. Fisk, and P. C. Canfield. Resistivity, magnetization, and specific heat of $YbAgCu_4$ in high magnetic fields. *Phys. Rev. B*, 51(21):15053, 1995.

[27] C. Rossel, K. N. Yang, M. B. Maple, Z. Fisk, E. Zirngiebl, and J. D. Thompson. Strong electronic correlations in a new class of Yb-based compounds: $YbXCu_4$ (X = Ag, Au, Pd). *Phys. Rev. B*, 35(4):1914, 1987.

[28] I. Felner and I. Nowik. First-order valence phase transition in cubic $Yb_xIn_{1-x}Cu_2$. *Phys. Rev. B*, 33(1):617, 1986.

[29] J. L. Sarrao, A. P. Ramirez, T. W. Darling, F. Freibert, A. Migliori, C. D. Immer, Z. Fisk, and Y. Uwatoko. Thermodynamics of the first-order valence transition in $YbInCu_4$. *Phys. Rev. B*, 58(1):409, 1998.

[30] V. Fritsch, J. D. Thompson, and J. L. Sarrao. Spin and orbital frustration in $RInCu_4$ (R = Gd, Dy, Ho, and Er). *Phys. Rev. B*, 71(13):132401, 2005.

[31] V. Fritsch, J. D. Thompson, J. L. Sarrao, H-A Krug von Nidda, R. M. Eremina, and A. Loidl. Correlation between magnetic frustration and electrical conductivity in $RInCu_4$ compounds (R = Gd - Tm). *Phys. Rev. B*, 73(9):094413, 2006.

[32] A. Doğan and R. Pöttgen. The ordered laves phases $CeNi_4Cd$ and $RECu_4Cd$ (RE = Ho, Er, Tm, Yb). *Zeitschrift für Naturforschung B*, 60(5):495–498, 2005.

[33] K. R. Lea, M. J. M. Leask, and W. P. Wolf. The raising of angular momentum degeneracy of f-electron terms by cubic crystal fields. *J. Phys. Chem. Solids*, 23(10):1381–1405, 1962.

[34] K. D. Schotte and U. Schotte. Interpretation of Kondo experiments in a magnetic field. *Phys. Lett. A*, 55(1):38–40, 1975.

[35] L. Balicas, S. Nakatsuji, H. Lee, P. Schlottmann, T. P. Murphy, and Z. Fisk. Magnetic field-tuned quantum critical point in $CeAuSb_2$. *Phys. Rev. B*, 72(6):064422, 2005.

[36] S. L. Bud'ko, P. C. Canfield, M. A. Avila, and T. Takabatake. Magnetic-field tuning of the low-temperature state of $YbNiSi_3$. *Phys. Rev. B*, 75(9):094433, 2007.

[37] E. Mun, S. L. Bud'ko, A. Kreyssig, and P. C. Canfield. Tuning low-temperature physical properties of $CeNiGe_3$ by magnetic field. *Phys. Rev. B*, 82(5):054424, 2010.

[38] O. Trovarelli, C. Geibel, S. Mederle, C. Langhammer, F. M. Grosche, P. Gegenwart, M. Lang, G. Sparn, and F. Steglich. $YbRh_2Si_2$: Pronounced non-Fermi-liquid effects above a low-lying magnetic phase transition. *Phys. Rev. Lett.*, 85(3):626, 2000.

[39] P. Gegenwart, J. Custers, C. Geibel, K. Neumaier, T. Tayama, K. Tenya, O. Trovarelli, and F. Steglich. Magnetic-field induced quantum critical point in $YbRh_2Si_2$. *Phys. Rev. Lett.*, 89(5):056402, 2002.

[40] S. L. Bud'ko, E. Morosan, and P. C. Canfield. Magnetic field induced non-Fermi-liquid behavior in YbAgGe single crystals. *Phys. Rev. B*, 69(1):014415, 2004.

[41] E. Mun, S. L. Bud'ko, C. Martin, H. Kim, M. A. Tanatar, J. Park, T. Murphy, G. M. Schmiedeshoff, N. Dilley, R. Prozorov, et al. Magnetic-field-tuned quantum criticality of the heavy-fermion system YbPtBi. *Phys. Rev. B*, 87(7):075120, 2013.

[42] H. v. Löhneysen, A. Rosch, M. Vojta, and P. Wölfle. Fermi-liquid instabilities at magnetic quantum phase transitions. *Rev. Mod. Phys.*, 79(3):1015, 2007.

[43] Q. Si. Quantum criticality and global phase diagram of magnetic heavy fermions. *physica status solidi (b)*, 247(3):476–484, 2010.

[44] Q. Si, S. Rabello, K. Ingersent, and J. L. Smith. Locally critical quantum phase transitions in strongly correlated metals. *Nature*, 413(6858):804, 2001.

[45] H. Shishido, T. Shibauchi, K. Yasu, T. Kato, H. Kontani, T. Terashima, and Y. Matsuda. Tuning the dimensionality of the heavy fermion compound $CeIn_3$. *Science*, 327(5968):980–983, 2010.

[46] M. Vojta. From itinerant to local-moment antiferromagnetism in Kondo lattices: Adiabatic continuity versus quantum phase transitions. *Phys. Rev. B*, 78(12):125109, 2008.

[47] T. Senthil, M. Vojta, and S. Sachdev. Weak magnetism and non-Fermi liquids near heavy-fermion critical points. *Phys. Rev. B*, 69(3):035111, 2004.